Physical Optics and Electronics

RLE Group
Physical Optics and Electronics Group

Academic and Research Staff
Professor Rajeev J. Ram, Dr. Xiaoyun Guo, Dr. Dietrich Lueerssen

Graduate Students
Gustavo Gil, Harry Lee, Kevin Lee, Tom Liptay, Peter Mayer, Tauhid Zaman

Technical and Support Staff
Catherine Bourgeoise

Overview

The research in the Physical Optics and Electronics Group is divided along three primary themes:

- Integrated Photonics
- Biophotonics and Bioprocess
- Thermodynamics of Semiconductor Devices

In all three areas the goal of this research is to exploit processes in physics to invent new devices that lead to better systems. Each researcher works to model and design a new device, implement the design, and then integrated this device into a system which defines the state-of-the-art.

Parallel Integrated Bioreactor Array

Sponsor
DuPont MIT Alliance

Project Staff
Harry Lee, Professor Rajeev J. Ram
Paolo Boccazzi, Professor Anthony J. Sinskey
Professor Klavs Jensen

We are developing a system to perform multiple microbial growth experiments in parallel with the aim of facilitating bioprocess development and fundamental studies of the dynamic response of microbes to changing conditions. Key attributes for such a system are the ability to provide individual pH control in each reactor; high oxygen transport rates to support aerobic growth to high cell density; in-situ measurement of culture parameters; ease of use, setup and maintenance; and scalability to large numbers of reactors. These attributes motivate a miniaturized solution and the design and integration of meso-scale fluidic devices.

Our integrated bioreactor combines a peristaltic oxygenating mixer [Ref last year RLE report] with a pair of metered fluid injectors. In combination, these devices allow individual pH control in four integrated bioreactors. A photograph and schematic view with cross sections is shown in Fig. 1. Fluid injectors are composed of a fluid reservoir sealed with a membrane, which can be deflected by pressurizing the chamber above. This generates a driving pressure to allow injection of fluid against a head pressure. Fluid is metered by actuating three valves in the fluid channel in sequence. The injected fluid is then mixed into the well in less than 15 seconds by the peristaltic oxygenating mixer. Fig. 2 shows titration curves of 100mM potassium phosphate (dibasic) measured using optical pH sensors and 270nL injections of 1M HCl and 1M NaOH. Titration

curves are repeatable and show a pH resolution of 0.06, which is sufficient for pH control of bioreactors.

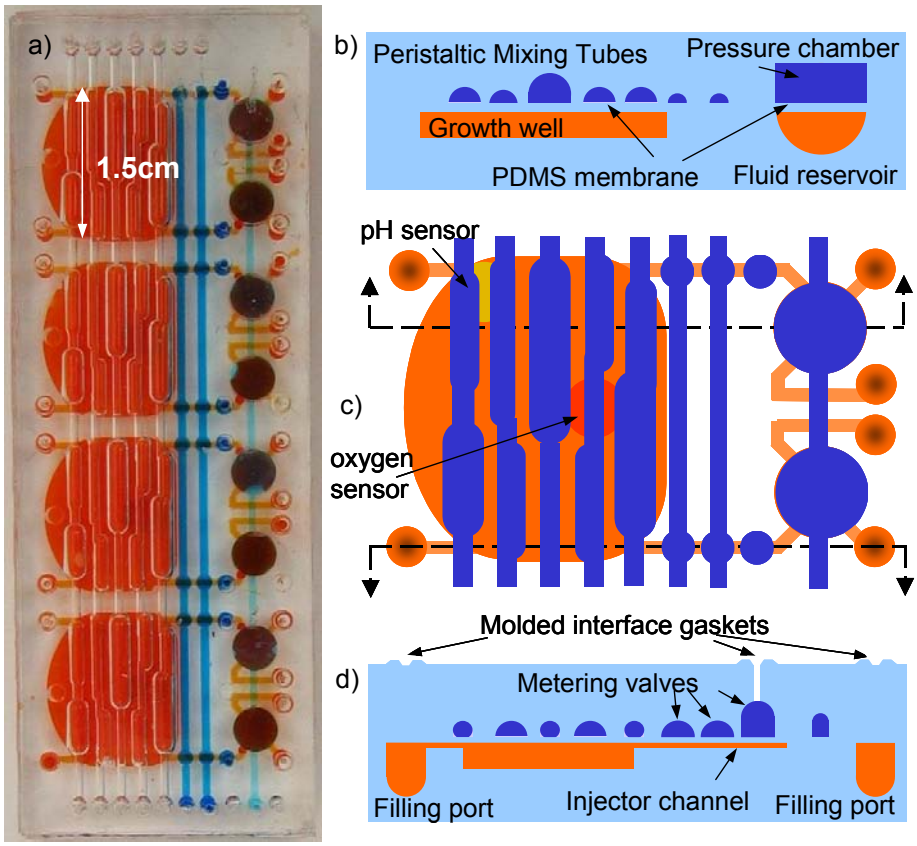

Figure 1. (a) Photograph: Pneumatic actuation of mixing tubes, two metering valves, and the pressure chamber is shared between the four devices for scalability. The third metering valve is independently actuated. (b) The pressure chamber and PDMS membrane allow a driving pressure to force the liquid into the injector channel and operate against backpressure, while maintaining sterility. (c) Sensors are fluorescence based. The growth well can hold 80-100μL of liquid and the injectors 15-25μL. d) Gaskets at all filling, or pneumatic actuation ports are molded into the device for easy world-to-chip interfacing. Metering valves are normally pressurized. The actuation sequence 100, 101, 001, 011, 111, injects approximately 270nL into the growth well.

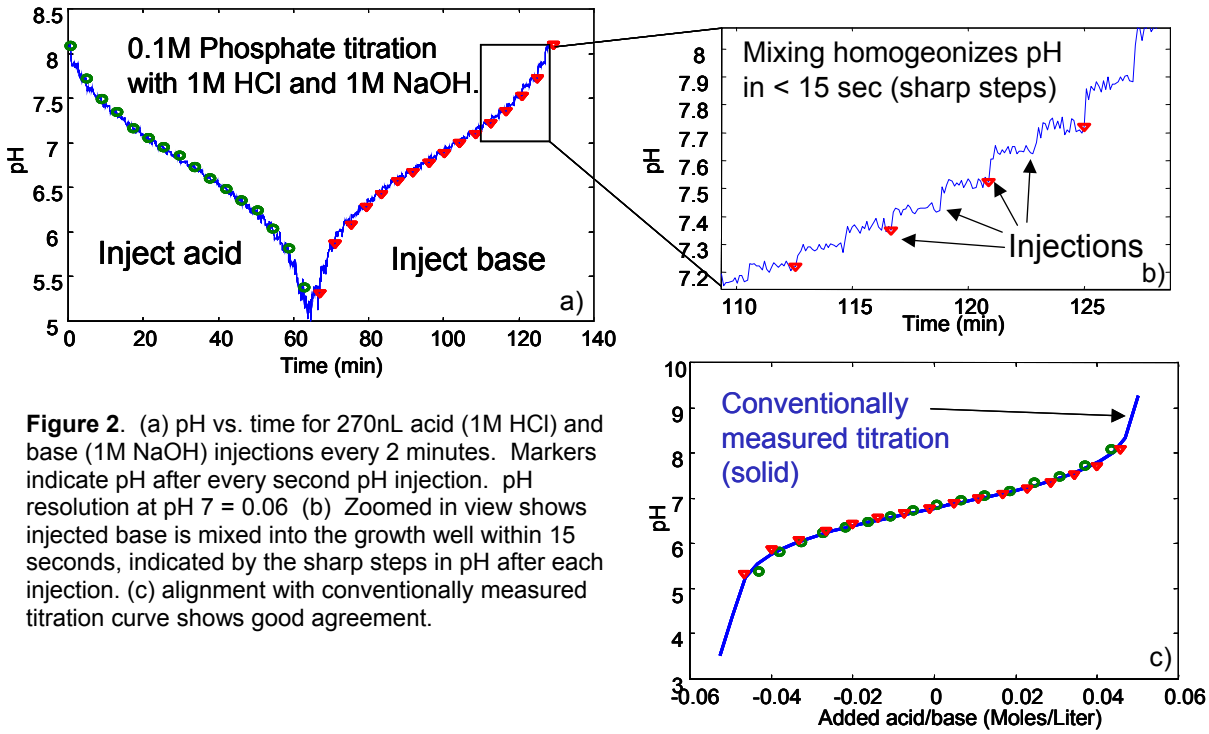

Figure 2. (a) pH vs. time for 270nL acid (1M HCl) and base (1M NaOH) injections every 2 minutes. Markers indicate pH after every second pH injection. pH resolution at pH 7 = 0.06 (b) Zoomed in view shows injected base is mixed into the growth well within 15 seconds, indicated by the sharp steps in pH after each injection. (c) alignment with conventionally measured titration curve shows good agreement.

Large-area Polymer Waveguides for Integrated Biosensors

Sponsor
DuPont MIT Alliance

Project Staff
Kevin Lee, Professor Rajeev J. Ram

Fluorescence spectroscopy is a widely used method for determining environmental parameters for biological systems. Biological systems, striving for 'lab-on-a-chip' behavior, benefit greatly from optical sensing techniques that can provide real time monitoring capabilities without disturbing a system's equilibrium. While most integrated biological chips are small in themselves, the optics necessary for using optical sensors remain large and often require precise alignment. In order to reduce the amount of external optics, optical components should be integrated onto the biochip itself.

For optical integration of biosensors to succeed, three optical components are required. These are large area waveguides for delivery and collection, filters for attenuation of unwanted signals, and light sources for sensor excitation. In order to create waveguides, square 800μm wide PDMS microchannels were injected with UV-curable polyurethane (Norland Optical Adhesive 63). Straight waveguides exhibited losses of 0.28 dB/cm at 626 nm and 0.65 dB/cm at 470 nm as shown in Fig. 3(a). Losses of this magnitude were considered to be acceptable with respect to the size of a biochip, which is typically no more than a few centimeters.

To create filters, optically absorbing dyes were dissolved into NOA and the resulting solution was injected and cured to form a waveguide structure. The absorption spectrum, in Fig. 3(b), shows the absorption contribution due to just the dye. By dissolving an absorbing dye into the waveguide core, both low-loss transmission of collection signals and attenuation of excitation signals can be achieved. The same method used to create waveguide filters can also be used to create light sources. By embedding quantum dots into polyurethane, waveguides were made with high fluorescence characteristics. Preliminary experiments into this method demonstrated an efficiency of 0.1% in the ability to convert UV light into guided visible light. A picture of a quantum dot waveguide output is shown in Fig. 4.

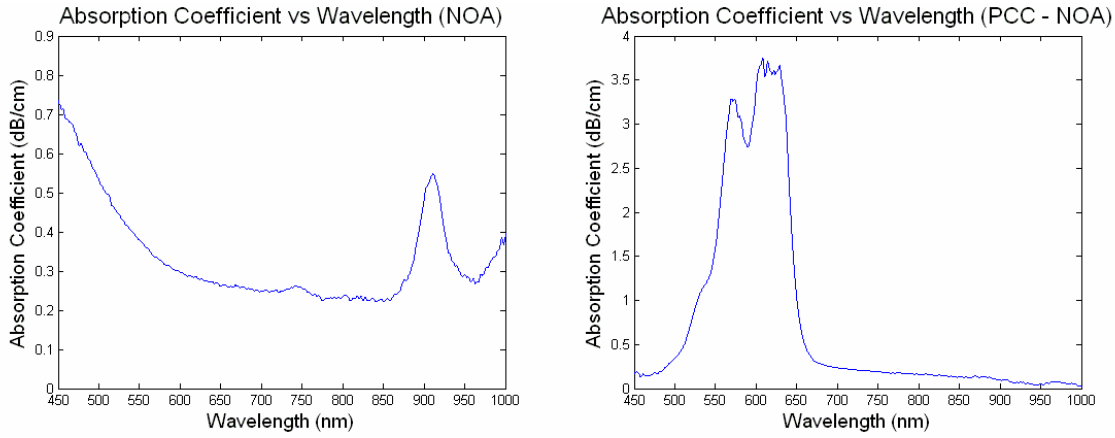

Fig. 3: Graphs of the absorption coefficient for two NOA waveguide. (a) Shows a waveguide with only NOA. The increase in absorption with decreasing wavelength is due to the NOA, which becomes absorptive at ultraviolet wavelengths. (b) Shows a waveguide with embedded filtering characteristics. The peak in absorption between 500 nm and 650 nm is due to Pinacyanol Chloride; where as the rest of the graph closely resembles that of a regular NOA waveguide.

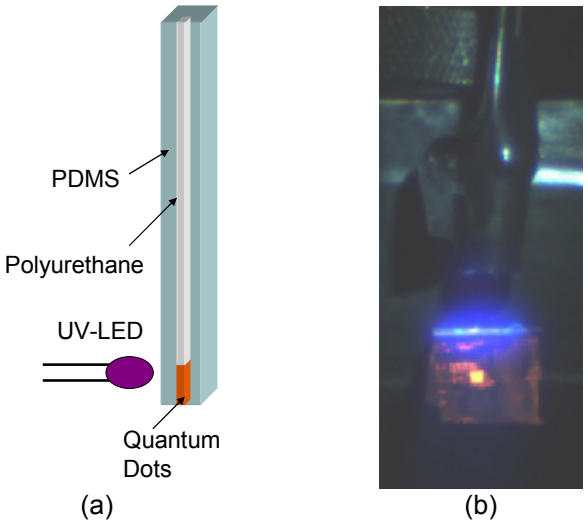

Fig. 4: (a) shows a schematic of the fabricated quantum dot waveguide. An ultraviolet LED is used to excite the waveguide from the side. An image of the quantum dot emission at the end of the waveguide is shown in (b).

On-line Monitoring of Plant and Microbial Bioreactions

Sponsors
The Dupont-MIT Alliance
The Malaysia-MIT Biotechnology Partnership Programme

Project Staff
Gustavo Gil, Harry Lee, Rajeev Ram

Raman spectroscopy is a fast growing technique for non-invasive biomonitoring applications. A Raman spectrum is acquired by observing the inelastically scattered photons from a sample illuminated by narrowband excitation, such as a laser, via a spectrometer. Recent technological innovations in holographic optical notch filters, NIR semiconductor lasers, and fiber optic probes, have made Raman spectroscopy more cost effective, while the low Raman signature of water and glass have made it well suited for noninvasive biological applications, such as on-line bioprocess monitoring.

Improvements to a previously built Raman bioprocess monitoring assembly were done to improve error performance, reduce model errors, and better understand the advantages and limitations of the technology. The calibration procedure was redesigned to eliminate non-scalar distortions caused by perturbations of the setup parameters. Laser-line drift and vibration problems were eliminated by including the Rayleigh (785nm) line as an internal wavelength standard. A more rigorous error analysis was implemented to take into account errors in the calibration spectra due to shot noise in the electronics. A comparison of both online and offline results with liquid chromatography (HPLC) of Phenylalanine production in an *E. coli* fermentation is shown in Figure 5. Additionally, offline Raman spectra of oil palm (*Elaeis guineensis*) cultures were tested for possible portability of the technique to plant cell bioreactions. Concentration estimates of sucrose, fructose, and glucose were made, showing good agreement with HPLC, as can be seen in Figure 6. Since there is less trouble from scattering in plant cell cultures, this experiment shows that an on-line Raman monitoring setup is well suited for plant cell cultures as well.

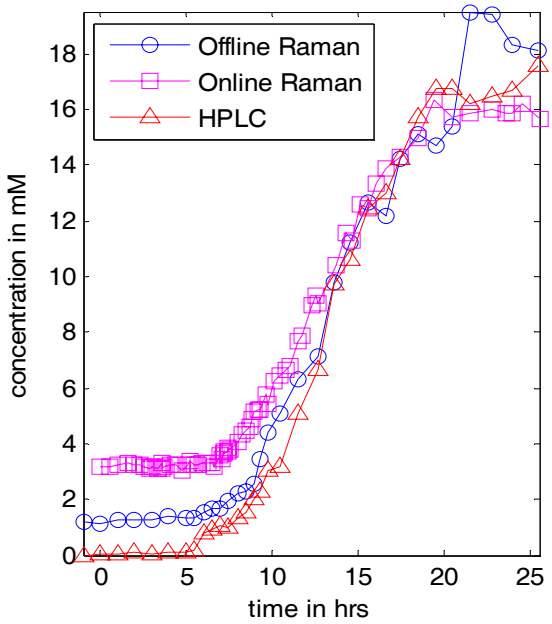

Figure 5: Estimation of Phenylalanine using HPLC(triangles), and Raman spectroscopy online (squares) and offline (circles)

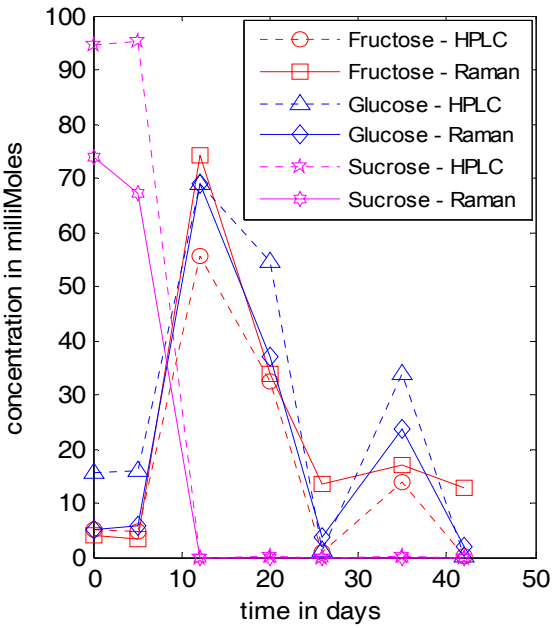

Figure 6: Concentration estimation of sucrose (magenta), fructose (red), and glucose (blue)

Spectral Analysis of Colloidal Quantum Dots

Sponsors
Packard Foundation
Center for Materials Science and Engineering (NSF-MRSEC)

Project Staff
Tom Liptay, Professor Rajeev J. Ram

For many applications of nanocrystals (NCs), including optical barcodes, displays, and laser gain media, the linewidth of the NC spectrum is an important design parameter. We have combined various broadening mechanisms – acoustic and optical phonon broadening, optical phonon replicas, and energy level occupation - into a single model in order to predict the linewidth of an individual CdSe/ZnS NC at room temperature (RT), where most NC applications will be used. All of the parameters in our model are determined from experimental results from the literature in the low/mid temperature regime. Figure 7 shows the contributions to the total RT linewidth versus NC radius. We find that acoustic phonon broadening dominates for small NCs, while optical phonon broadening dominates for large NCs.

We have also measured the temperature dependence of emission for 4 NC ensembles as a function of temperature. The temperature dependence is less than expected from our model. Figure 8 shows the linewidth of the ensembles at RT (red) and the extracted NC homogeneous linewidth (black). The most uncertain parameter in our model is the strength of optical phonon broadening. We theorize that the optical phonon coupling constant B is reduced to about 10% of its value in bulk. Our data indicates that it is possible to reduce the RT ensemble linewidth of our samples to less than half by minimizing NC inhomogeneities.

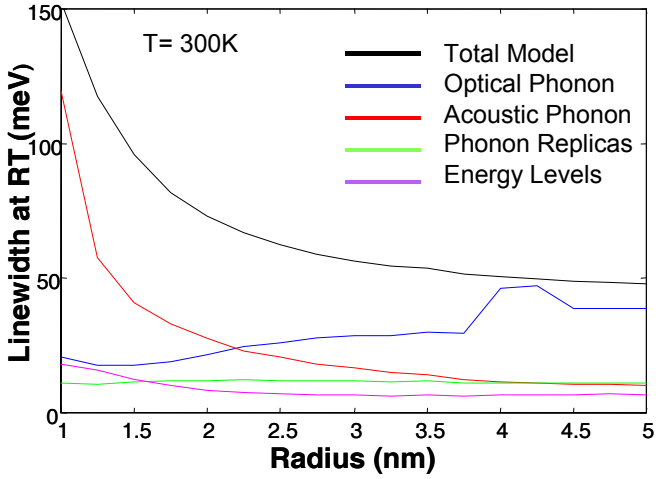

Figure 7: Shown is the expected RT linewidth versus NC radius (black). Our model is based on parameters that have been measured in the low/mid temperature regime for CdSe NCs. The colored plots are calculated by turning off a broadening mechanism in our model and then subtracting the result from the total model.

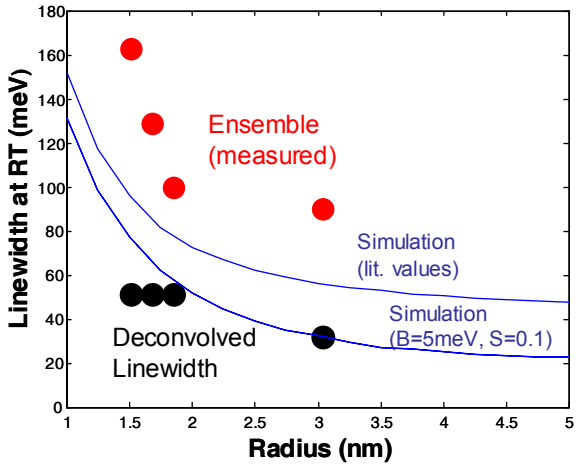

Figure 8: Red – ensemble RT PL linewidth. Black – Assuming that the low temperature ensemble PL linewidth is entirely due to inhomogeneities between NCs, the RT homogeneous linewidth can be estimated by assuming that the temperature dependence is due increasing homogenous linewidth. Dashed – our model with reduced optical phonon coupling B.

High Index Contrast Waveguides in Indium Phosphide

Sponsors
DARPA

Project Staff
Dr. Xiaoyun Guo, Tauhid Zaman, Professor Rajeev J. Ram

An optical isolator is a device that transmits light in only one direction. Optical isolators are required in optical communication systems to protect laser sources from back reflections. A waveguide isolator which can be integrated with the source and other waveguide devices is essential to large scale photonic integration. Currently available microoptic isolators are bulky and require expensive alignment. An isolator on III-V semiconductor substrates such as InP, will be most beneficial for large scale photonic integration.

A simplest type of isolator is composed of a Faraday rotator between two polarizers set at 45°with respect to each other. The non-reciprocal polarization rotation, induced by a Faraday rotator, is the key for such device. In Faraday rotation, the coupling between TE and TM mode determines the efficiency of the polarization rotation. To achieve maximum Faraday rotation effect, one needs to minimize the difference of propagation constants. Realization of integrated Faraday rotators requires a waveguide where TE and TM modes have nearly equal propagation constants. To achieve low enough birefringence waveguide has been a challenge for waveguide isolator using Faraday rotation effect. And thus most researchers turn to exploit the nonreciprocal phase shift for waveguide isolator development, despite many advantages to use Faraday effect in isolator design.

Unlike iron garnet, such as YIG, with many sources of birefringence, one only needs to consider geometric birefringence in InP/InGaAsP. Other sources are small enough to be neglected. The geometry of the waveguide was designed through theoretical calculation. The waveguide is 1.4μm wide and 2.5μm deep. The waveguide was fabricated with low pressure methane based reactive ion etching. The waveguides consist of a 0.5μm Fe-doped InGaAsP core layer and 1μm Fe-doped InP cladding layers. To achieve appreciable Faraday rotation for the Verdet coefficients measured above, the difference of effective refractive index between TE and TM modes was calculated to be less than 10^{-5}.

In the birefringence measurement, a beam splitter was used to split the TE and TM mode of the output light. Together with the waveguide simulation, the birefringence can be calculated from the measurement. The TE and TM modes have different effective refractive indices, which will cause the transmission peaks wavelengths of the two modes to be different. The transmission spectrum will give the information on refractive index for both mode (assuming their difference induce less than π phase change near the calculated zero birefringence point) :

$$\Delta n = n_{TE} - n_{TM} = n_{TE}(1 - \frac{\lambda_{TM}}{\lambda_{TE}})$$

where λ is the wavelength and n is the refractive index.

The zero birefringence wavelength for waveguide with 1.4μm width is calculated to be 1540nm. The birefringence around the calculated zero birefringence wavelength of this waveguide is also measured.

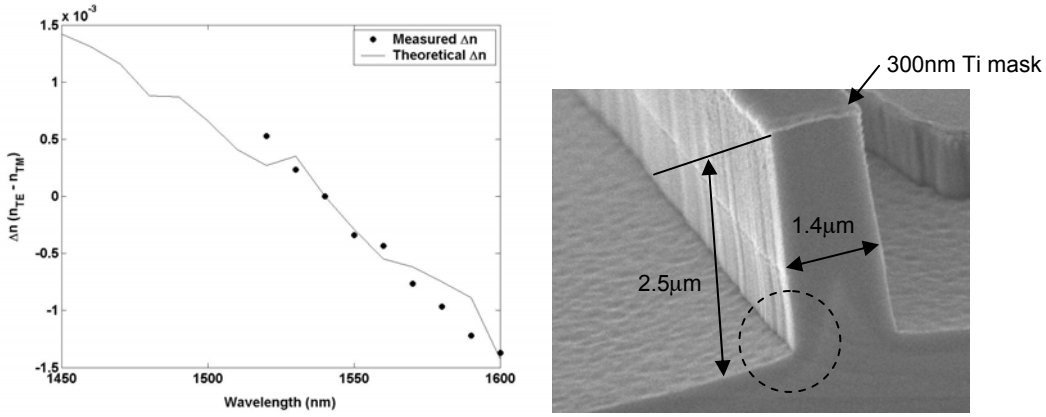

(a) (b)

Fig. 9 (a) Birefringence of the waveguide vs. measured wavelength. The solid line is theoretical calculation curve and the dots are experimental data. (b) Etched waveguide geometry.

The measured birefringence agrees with the theoretical simulation very well. The lowest birefringence is measured at 1540nm. The birefringence is less than 10^{-5}, satisfying the requirement for waveguide Faraday rotator. It confirms the feasibility of eliminating waveguide birefringence by proper structural design and RIE high mesa etching. The achievement of low enough birefringence waveguide further confirms the feasibility of realizing waveguide isolator using Faraday effect.

Future work will be done on decreasing the waveguide loss and device characterization.

Integrated Optical Isolator and Circulator

Sponsor
DARPA

Project Staff
Tauhid Zaman, Professor Rajeev Ram

Optical isolators are devices that allow light propagation in only one direction. They are required in optical communication systems to protect laser sources and optical gain elements from back-reflections which cause noise and instabilities. Available micro-optic isolators are bulky and require expensive alignment. A waveguide isolator which can be integrated with the source and other waveguide devices will be necessary for large scale photonic integration.

We present a design for a fully integrated, polarization independent, compact optical isolator. The isolator, shown in Figure 10, is composed of 3dB power splitters, half-wave plates, and Faraday rotators. This architecture is based on that of Sugimoto [1], except that we have put all of the bulk optical components into waveguide forms suitable for photonic integration. Each component is composed of a 1.0 μm InP cladding surrounding a 0.5 μm InGaAsP core. The overall isolator fabrication process is relatively simple, requiring only two etch steps.

Input light on the left side of the isolator will be split by the power splitter and sent through the two arms. At the right power splitter, the two arms are in phase and interfere constructively, which results in light from port 1 exiting at port 3, and light from port 2 exiting at port 4. In the reverse direction, input light on the right side of the isolator is split by the power splitter, and at the left power splitter the two arms are out of phase. This results in light from port 3 exiting at port 2, and light from port 4 exiting at port 1. This non-reciprocal phase shift results from this specific combination of non-reciprocal Faraday rotators and reciprocal half-wave plates. Because this non-reciprocal phase is the result of polarization rotation, it is the same for any input polarization, thus giving polarization independent operation. If only 2 ports are utilized, this device functions as an isolator. However, if all 4 ports are used, it acts as a circulator.

The power splitting is achieved with a multimode interferometer (MMI). It utilizes the interference of guided modes to split the power into its two arms. The MMI is 3.4 μm wide and 52 μm long.

The Faraday rotator is achieved by using a zero-birefringence waveguide composed of a magneto-optic material. For our device, the magneto-optic material is iron doped InGaAsP. The waveguide width to achieve zero-birefringence is 1.4 μm. The device length depends on the Verdet coefficient or rotational power of the magneto-optic material. A 45° rotation is required, so if a Verdet coefficient of 100 °/mm is assumed, then the Faraday rotator length is 450 μm.

To achieve the integrated half-wave plates, an asymmetric waveguide was needed. This would ensure that eigenmode polarizations, or fast and slow axes, were not horizontal and vertical. By etching a notch on top of the core, this asymmetry could be achieved, and by tuning the width of this notch, we could control the orientation of the fast and slow axis. We found that a 0.85 μm notch would give the desired slow axis angle of 22.5° with respect to the horizontal. The integrated half-wave plate is then 157.5 μm in length.

Combining all these elements, we find that the isolator length is 711.5 μm. The isolator shows a maximum isolation of 23 dB and maintains a minimum isolation of 12 dB over a 100 nm bandwidth for both TE and TM polarizations, as shown in Figure 11. The main factors limiting maximum isolation and maximum bandwidth are the birefringence in the Faraday rotators and the power imbalance in the MMI's. The numerical simulation was performed using code developed by Mike Watts and Hermann Haus at MIT.

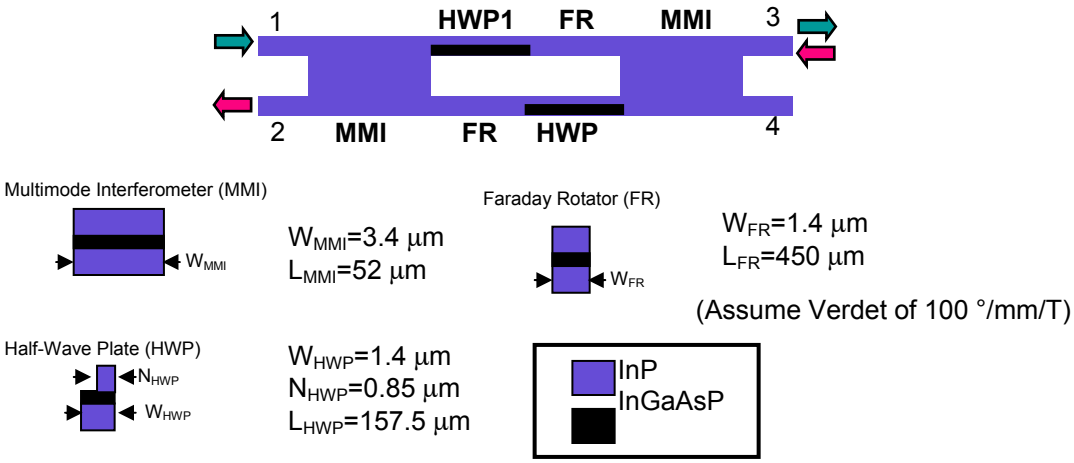

Figure 10: Integrated isolator design

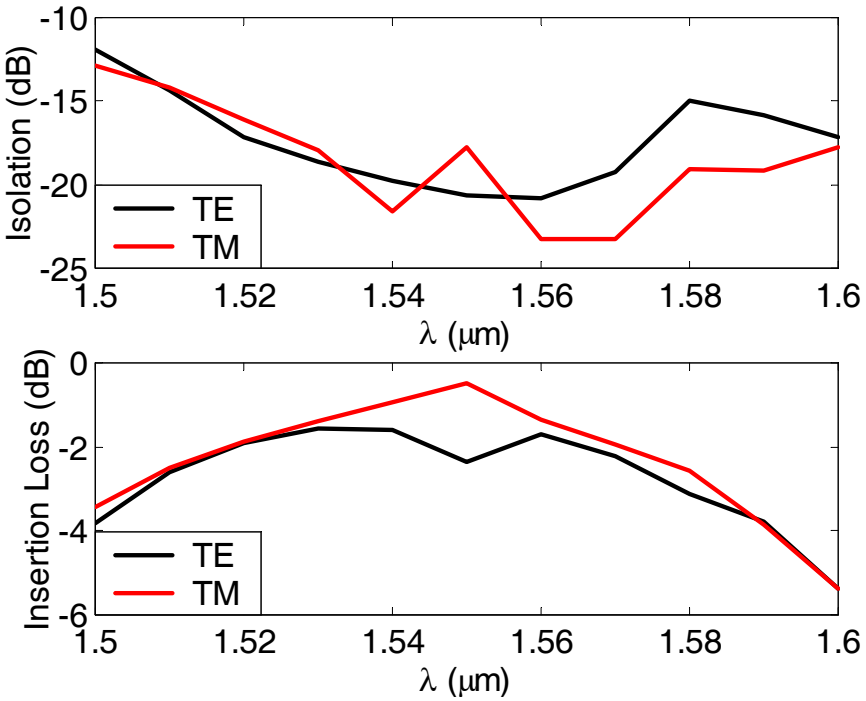

Figure 11: Isolation and insertion loss of integrated isolator

References

[1] N. Sugimoto, et. al.,*IEEE Photon. Tech. Lett.*, Vol. 11, No. 3, March 1999

Nanoscale Thermal Imaging Microscopy

Sponsors
Office of Naval research

Project Staff
Dr. Dietrich Lueerssen, Peter Mayer, Professor Rajeev J. Ram

Thermoreflectance microscopy is a form of modulation spectroscopy used to obtain images of the temperature distribution on the surface of a material. For most solids, a change in temperature produces a small but measurable change in the reflectance spectrum of the material (perhaps 1 part in 10^{-4}). By measuring the change in reflectance while modulating the temperature, the change in temperature can be inferred. This approach is useful for examining heat transport in electronic/optoelectronic devices, since the heating due to a changing bias current or voltage can be measured (Fig. 12 and Fig. 13).

A traditional thermoreflectance image is constructed using a laser, a single photodetector, and a lock-in amplifier. The laser is scanned slowly around the sample surface, allowing a temperature image to be constructed with a resolution equal to that of the laser spot size. In our setup, the entire field of view is illuminated with an LED, and a CCD camera is used to acquire the entire field of view simultaneously. To obtain high temperature resolution (~10 mK), two unusual methods are used: first, the CCD is used as a multichannel lock-in detector by triggering the camera four times per period of the temperature oscillation of the sample. Second, the phenomenon of noise induced threshold crossing is used to break the dynamic range barrier of the CCD camera set by the quantization bin size. Because the measurement is non-contact it is free of artifacts from parasitic heat leaking through the contacting element. Because the reflectance of the device is measured with visible light (or even UV), the maximum (Rayleigh-limit) spatial resolution is greater than that obtained from traditional IR-imaging systems. These two features make it very promising for the thermal imaging of nanoscale devices and phenomena.

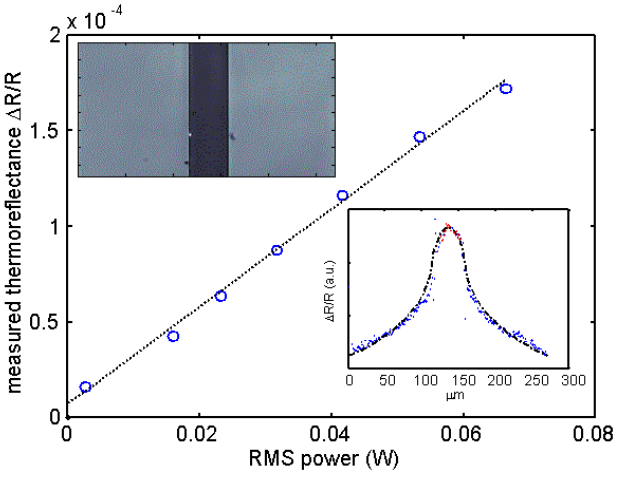

Fig. 12. Temperature change of a diffused resistor due to Joule heating.

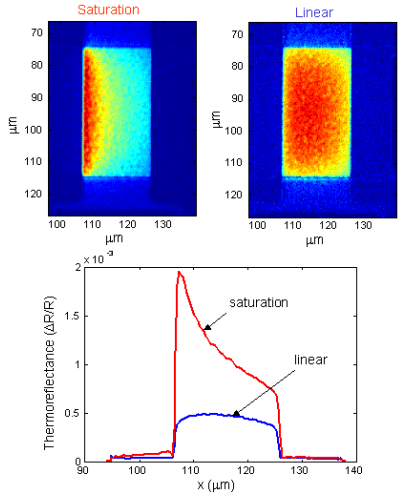

Fig. 13. Temperature profile in the polysilicon gate of a FET transistor for linear and saturation regime bias.

Publications

Dietrich Lueerssen, Janice A. Hudgings, Peter M. Mayer, and Rajeev J. Ram, "Nanoscale Thermoreflectance with 10 mK Temperature Resolution Using Stochastic Resonance," 21st IEEE SEMI-THERM symposium, San Jose, California, March 15-17, 2005.

High Power Density Thermoelectric Generators

Sponsors
Office of Naval research

Project Staff
Peter Mayer, Professor Rajeev J. Ram

Thermoelectric power generation is a means of converting heat power into electrical power quietly and with no moving parts. Many recent advances in thermoelectrics have focused on the nanoscale engineering of thin-film materials for higher thermoelectric figure of merit (Z). In a thermoelectric (TE) generation system, attaining the performance enhancements promised by the large material figure of merit of the thin-films presents a formidable challenge: the temperature dropped across the thin-film must be maximized while managing a thermal and electrical flux tens or hundreds of times greater than that of conventional devices.

With this in mind, we have made a systems-level investigation on proper materials selection, impedance matching, heat spreading, and actively chilled heat sinks with respect to their impact on overall system efficiency and the device operating point. Substantial improvements are possible using these techniques provided that the additional the electrical parasitics introduced can be managed (Fig 14). An experimental investigation of several thin film and nanostructured thermoelectric devices is currently underway. Measurements on BiTe thin-film devices (obtained from Marlow industries) with > 1 W/cm^2 of generated power are shown in Fig 15.

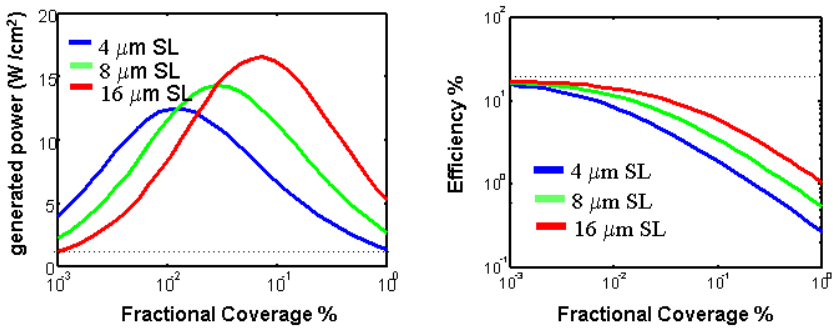

Fig 14. Effect of variations in TE leg length and heat spreading on system performance, as parametrized by the fractional coverage of a diamond substrate.

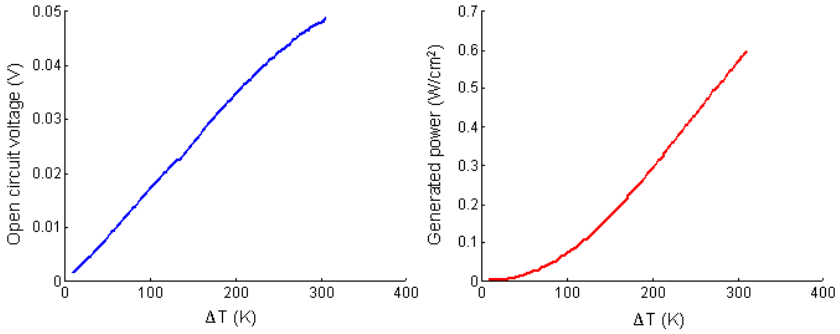

Fig 15. Measured open circuit voltage (related to Seebeck coefficient) and output power of BiTe-based powder metallurgy sample leg under optimum power generation load.